

Supporting Information for

Command of three-dimensional solitary waves via photopatterning

Chao-Yi Li^{a,b,1}, Xing-Zhou Tang^{c,1}, Xiao Yu^a, Noe Atzin^c, Zhen-Peng Song^b, Chu-Qiao Chen^c, Nicholas L. Abbott^d, Bing-Xiang Li^{a,b,*}, Juan J. de Pablo^{c,e,*}, Yan-Qing Lu^{a,*}

^aNational Laboratory of Solid State Microstructures, College of Engineering and Applied Sciences, and Collaborative Innovation Center of Advanced Microstructures, Nanjing University, Nanjing 210093, China.

^bCollege of Electronic and Optical Engineering & College of Flexible Electronics (Future Technology), Nanjing University of Posts and Telecommunications, Nanjing 210023, China.

^cPritzker School of Molecular Engineering, The University of Chicago, Chicago, Illinois 60637, USA.

^dSmith School of Chemical and Biomolecular Engineering, Cornell University, Ithaca, New York 14853, USA.

^eCenter for Molecular Engineering, Argonne National Laboratory, Lemont, Illinois 60439, USA.

¹C.L. and X.T. contributed equally to this work

*Corresponding author: Bingxiang Li, Juan J. de Pablo, Yanqing Lu

Email: bxli@njupt.edu.cn, depablo@uchicago.edu, yqlu@nju.edu.cn

This PDF file includes:

Supporting text
Figures S1 to S11
Legends for Movies S1 to S9
SI References

Other supporting materials for this manuscript include the following:

Movies S1 to S9

Supporting Information Text

1: Detail of photopatterning

Photoalignment is one of the most powerful ways to control liquid crystal (LC) alignment, which employs light-matter interaction that the orientation of alignment depends on the polarization of the exposure light. To realize programmable director distribution of LCs, Liquid-crystal display (LCD) projectors were used to project light patterns (1). To regulate the direction of linear polarization of light, the combination of polarizer, LCD projector, and quarter-wave plates or two LCD projectors are required. The use of LCD projector (1) is elegant and that inspire us to build a micro-lithography system based on a digital-micro-mirror-device (DMD). Both DMD and LCD can be used for our work. In this work, we use DMD equipment in our laboratory.

Our photo-patterning technique based on a DMD micro-lithography system allows us to fabricate arbitrary two-dimensional geometry of surface boundary conditions for $\hat{\mathbf{n}}(\mathbf{r})$. As schematically shown in Fig. S1A, a UV light generated by LED is projected through the DMD with 1920×1080 pixels. The light part of a binary image can command DMD to open corresponding mirrors that reflect the UV light. The reflected light propagates through the polarizer and objective, then shining on sample with some polarization, P_c . In conclusion, images imported into the DMD control the boundary of surface alignment. The orientation of alignment ψ , which is perpendicular to P_c , are under the control by rotating the polarizer. To obtain the two-dimensional patterns with desired director distribution in this work, we adopt multi-step illuminations, namely, synchronously commanding the update of exposure images and the polarization direction of polarizer (*SI Appendix*, Fig. S1B-H). In this process, we need to guarantee the focus plane of objectives coincide the middle plane of the cell. The practical size of patterns varies from $10\ \mu\text{m}$ to $10\ \text{mm}$, which is related to the magnification of objectives and the size of binary image, for instance, Olympus objective with a $10\times$ magnification and image with 1920×1080 pixels yield a maximized dimension of $2.0\ \text{mm} \times 1.1\ \text{mm}$ in our system.

2: Detail of Landau-de Gennes model

We quantify the nematic order through a traceless, symmetric tensor:

$$Q_{ij} = s \left(\frac{3}{2} n_i n_j - \frac{1}{2} \delta_{ij} \right), \quad [\text{S1}]$$

where s is the degree of uniaxial nematic order. In order to avoid the confusion caused by the irregularity such as topological defects, we prefer to use the \mathbf{Q} tensor to describe the system. In our model, alternating current field (AC) couples to the director of the liquid crystal by a negative anisotropy of the permittivity. The liquid crystal is confined between two optical sensitive layers. These layers, exposed by UV light with different wavelengths ($\lambda = 365 \text{ nm}$ or $\lambda = 405 \text{ nm}$), exhibit different azimuthal anchoring energy. The surface difference is created by changing the elastic constant of layers in our model.

The system's free energy is expressed as follows:

$$\mathcal{F} = \int d^2r (f_{\text{LdG}} + f_{\text{elas}} + f_{\text{diel}} + f_{\text{flex}}). \quad [\text{S2}]$$

In this equation, the free energy density is a sum of four terms: the Landau–de Gennes thermal energy term (f_{LdG}), a contribution of elasticity (f_{elas}), a dielectric energy contribution (f_{diel}), and a term describing the contribution of flexoelectricity (f_{flex}).

The Landau–de Gennes thermal energy term f_{LdG} , also referred to as the enthalpic contribution (2,3), is expressed as:

$$f_{\text{LdG}} = \frac{1}{2} A \text{Tr}(\mathbf{Q})^2 + \frac{1}{3} B \text{Tr}(\mathbf{Q}^3) + \frac{1}{4} C (\text{Tr}(\mathbf{Q})^2)^2. \quad [\text{S3}]$$

Here, A , B , and C represent thermotropic coefficients. This term describes the nematic to isotropic second-order phase transition with increasing temperature and consists of an expansion of the free energy in powers of \mathbf{Q} .

The elastic energy models the elasticity of the nematic phase, and represents the LdG counterpart to the Frank-Oseen free energy density. It's a combination of splay, twist, and bend in a uniaxial limit, which is known as Frank-Oseen free energy. It can be written as:

$$f_{\text{O-F}} = \frac{1}{2} K_{11} S^2 + \frac{1}{2} K_{22} T^2 + \frac{1}{2} K_{33} B^2. \quad [\text{S4}]$$

In this equation, S , T , and B represent splay, twist, and bend, respectively (4).

The most general form that we employ (4-6) includes all gradient terms of quadratic order in \mathbf{Q} allowed by symmetry, plus one term at cubic order, and can be written as:

$$f_{elas} = \frac{L_1}{2} \frac{\partial Q_{ij}}{\partial x_k} \frac{\partial Q_{ij}}{\partial x_k} + \frac{L_2}{2} \frac{\partial Q_{ij}}{\partial x_j} \frac{\partial Q_{ik}}{\partial x_k} + \frac{L_3}{2} \frac{\partial Q_{ik}}{\partial x_j} \frac{\partial Q_{ij}}{\partial x_k} + \frac{L_6}{2} \frac{\partial Q_{ij}}{\partial x_l} \frac{\partial Q_{ij}}{\partial x_k}, \quad [S5]$$

where Einstein summation over repeated indices is implied, L_1 to L_6 are the elastic constants. Here we ignore the chirality.

The dielectric energy contribution is given by (7,8)

$$f_{diel} = -\frac{1}{2} \varepsilon_0 \varepsilon_{ij} E_i E_j, \quad [S6]$$

where ε_0 represents the dielectric permittivity of vacuum, and ε_{ij} corresponds to the tensorial dielectric permittivity of the nematic material:

$$\varepsilon_{ij} = \varepsilon_{\perp} \delta_{ij} + (\varepsilon_{\parallel} - \varepsilon_{\perp}) n_i n_j, \quad [S7]$$

here, ε_{\perp} and ε_{\parallel} are the dielectric permittivity perpendicular and parallel to the nematic field, respectively. By introducing an isotropic dielectric permittivity $\bar{\varepsilon}$ and a permittivity anisotropy $\varepsilon_a = \varepsilon_{\parallel} - \varepsilon_{\perp}$, one has $\varepsilon_{ij} = \bar{\varepsilon} \delta_{ij} + \varepsilon_a Q_{ij}$ (9,10).

The above expressions can be rewritten in terms of the \mathbf{Q} -tensor as:

$$f_{diel} = -\frac{1}{2} \varepsilon_0 (\bar{\varepsilon} \delta_{ij} + \varepsilon_a Q_{ij}) E_i E_j. \quad [S8]$$

In materials with $\varepsilon_a > 0$, the liquid crystal aligns with the electric field. In cases where ε_a is negative, the alignment is transverse. Our model requires a negative dielectric permittivity, which ensures that the director field aligns along the x-y plane (perpendicular to the electric field) rather than along the z-axis (the direction of the electric field). The system is subject to a sinusoidal electric field with frequency ω and maximum voltage E_0 along the z-axis, represented as $E = E_0 \sin(\omega t) \hat{z}$.

For bent-core molecules, the curvature-induced flexoelectric polarization of the material can be incorporated by adding the term to the electric displacement \mathbf{D} (11-13).

$$P_f = c_1 \partial \cdot \mathbf{Q} + c_2 \partial(\mathbf{Q} \cdot \mathbf{Q}) + c_3 \partial(\text{Tr} \mathbf{Q}^2) + c_4 [\mathbf{Q} \cdot (\partial \mathbf{Q}) - (\mathbf{Q} \cdot \partial) \cdot \mathbf{Q}]. \quad [S9]$$

The coefficients $c_{1...4}$ are defined in reference (11). Consequently, the flexoelectricity term, f_{flex} , can be expressed as:

$$f_{\text{flex}} = -\frac{4}{3}\chi_0 E_i \partial_j Q_{ij} - \frac{4}{3}\chi_+ E_i \partial_j (Q_{ik} Q_{jk}) - \frac{1}{3}\chi_2 E_k \partial_k (Q_{ij} Q_{ij}) - \frac{4}{9}\chi_- E_i (Q_{ik} \partial_j Q_{jk} - Q_{jk} \partial_j Q_{ik}).$$

[S10]

In the general case where the gradient of the nematic order parameter is neglected, the χ_2 term can be disregarded, however in this study, this term does not disregard. The χ_- term plays a key role in enhancing splay and bend deformations of the director field, thereby amplifying any irregularities caused by surface imperfections, dust particles, or inhomogeneities, which contribute to the nucleation of solitary waves. The term χ_0 represents the impact of the electric field's gradient, while χ_+ acts as a cross-term, signifying the interplay between the gradient of the nematic parameter s and the electric field. Previous studies that ignoring the gradient of nematic order parameter have considered the e_{11} and e_{33} terms that represent flexoelectricity (13,14), reflecting the influence to splay and bend, where the polarization is given by $P = e_{11}(\hat{n} \nabla \cdot \hat{n}) - e_{33}(\nabla \times \hat{n}) \times \hat{n}$. We considered the χ_s to represent the influence of the nematic order parameter (12).

Finally, we consider the Maxwell's equation. We take j_i as the current density (15) and is represented as

$$j_i = \sigma(E_i + \varepsilon_{ikn} \frac{v_k}{c} B_n). \quad [\text{S11}]$$

Here, σ is the electric conductivity. In the second contribution (related to the magnetic field B_n), the achievable velocity of the nematics (v_k) is much smaller than c . In this work, we neglect the magnetic contribution.

Based on the Maxwell's equation, the E is given as

$$\begin{aligned} -\varepsilon_0(\partial_i \partial_i E_i + \varepsilon_a Q_{ij} \partial_i E_j) = & -\varepsilon_0 \varepsilon_a E_j \partial_i Q_{ij} + \frac{4}{3}\chi_0 \partial_{ij} Q_{ij} + \frac{4}{3}\chi_+ \partial_{ij} (Q_{ik} Q_{kj}) \\ & + \frac{1}{3}\chi_2 \partial_{ii} (Q_{jk} Q_{kj}) + \frac{4}{9}\chi_- (\partial_i Q_{ik} \partial_j Q_{kj} - \partial_i Q_{jk} \partial_j Q_{ij}) \end{aligned} \quad [\text{S12}]$$

The solution of the above equation requires repeated iterations over the grid at each time step. We follow many numerical studies (16-20) and experimental facts (21,22) to avoid this complication in assuming uniform E .

To model the temporal evolution of the material, we apply the following equations for dynamic relaxation:

$$\frac{\partial Q_{ij}(r, t)}{\partial t} = -\frac{1}{\gamma_1} \frac{\delta F}{\delta Q_{ij}(r, t)}, \quad [\text{S13}]$$

where γ_1 denotes the rotational viscosity. Hydrodynamic effects are not considered in this initial attempt to model nematic solitons.

3: Derrick-Hobart type of re-scaling analysis with the 2D and 3D dimensionalities

Consider a scalar field ϕ in a space of the 3D. The energy E of this field configuration can generally be expressed as the sum of the kinetic and potential energy contributions. For static solutions, the kinetic term $(\partial_t \phi)$ is zero, so the energy consists only the potential and gradient terms:

$$E = \int dx^3 \left[\frac{1}{2} (\nabla \phi)^2 + V(\phi) \right] \quad [\text{S14}]$$

Consider a scaling transformation where spatial coordinates are scaled by a factor λ , i.e. $x \rightarrow \lambda x$. Under this transformation, the field $\phi(x)$ transforms to $\phi(\lambda x)$.

Under the re-scaling, the gradient term and the potential term scale differently: the gradient term $(\nabla \phi)^2$ scales as λ^{-2} and the volume element dx^3 scales as λ^3 . Thus, total energy as a function of λ becomes:

$$E(\lambda) = \int dx^3 \left[\frac{1}{2} \lambda^{-2} (\nabla \phi)^2 + V(\phi) \right] \lambda^3 = \lambda \int dx^3 \left[\frac{1}{2} (\nabla \phi)^2 \right] + \lambda^3 \int dx^3 [V(\phi)] \quad [\text{S15}]$$

To find a stable configuration, the energy $E(\lambda)$ should be minimized at $\lambda = 1$. While taking the derivative of $E(\lambda)$ with respect to λ and setting it to zero does not hold for arbitrary potentials $V(\phi)$ and nontrivial field configurations, indicating that $E(\lambda)$ cannot have a minimum at $\lambda = 1$ unless specific conditions on V are met.

$$\left. \frac{d(E(\lambda))}{d\lambda} \right|_{\lambda=1} = \int dx^3 \left[\frac{1}{2} (\nabla \phi)^2 \right] + 3 \int dx^3 [V(\phi)] = 0 \quad [\text{S16}]$$

Since the energy does not have a stable minimum at $\lambda = 1$, no stable, static soliton solutions exist in dimensions three and higher. This means the field configuration would either spread out or collapse, rather than forming a stable localized entity.

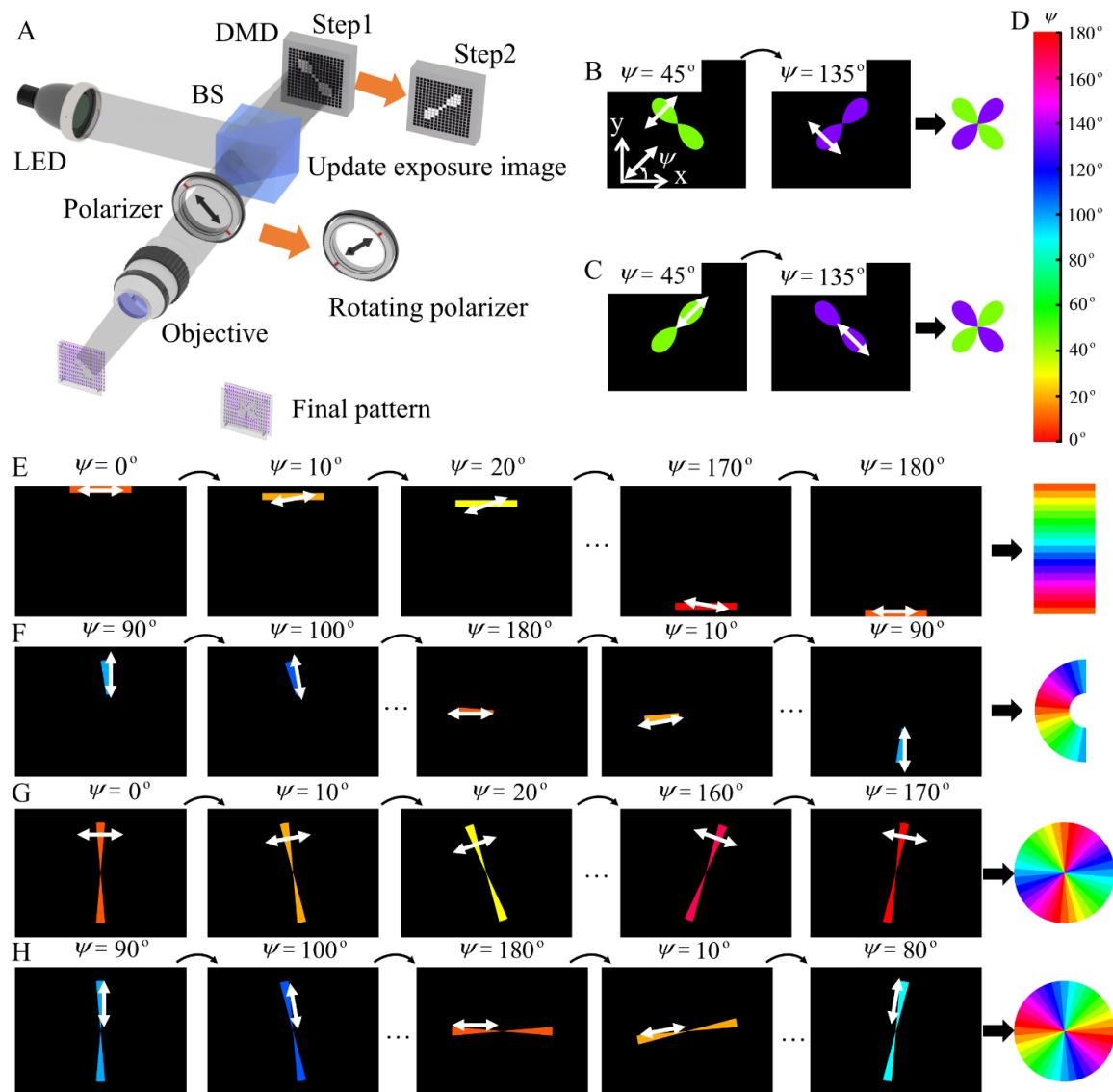


Fig. S1. Principles of photo-patterning of directrons machine guns. (A) the photoalignment technique based on a digital-micro-mirror-device. (B to D) utilizing double illuminations of patterns to generate directrons machine guns with binary director distribution. Double white arrow represents the orientation of nematic molecules. ψ is the azimuthal angle between orientation and x-axis. (E to H) production of directrons machine guns with vortices by multi-step exposure process.

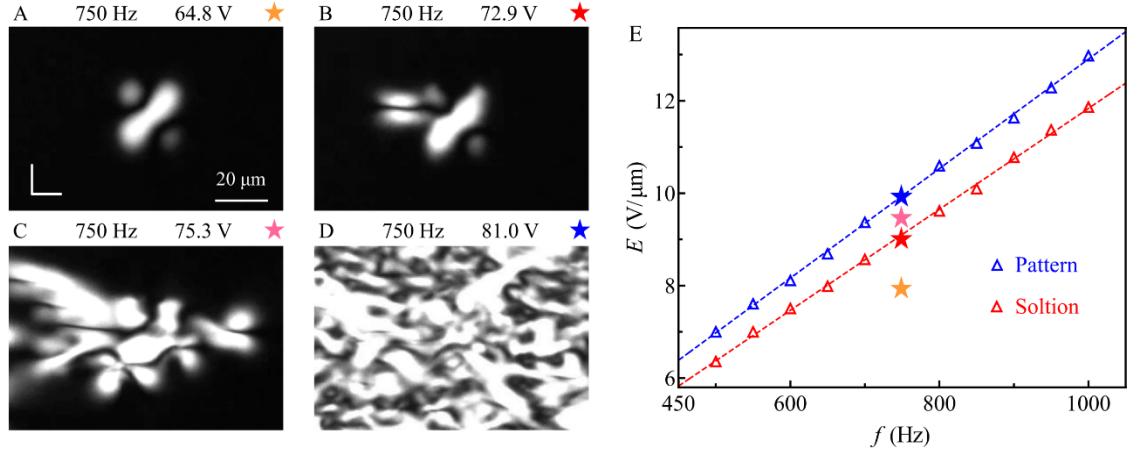


Fig. S2. Soliton properties as a function of the applied field. (A to D) Emergence and movement of directrons observed between crossed polarizers as the voltage U increases as indicated ($f = 750$ Hz , 55°C , $d = 8.1 \mu\text{m}$). (E) Frequency dependencies of threshold voltages required to generate directrons and patterns. Different colored pentagrams in the f - E state diagram indicate the electric field conditions corresponding to (A) to (D).

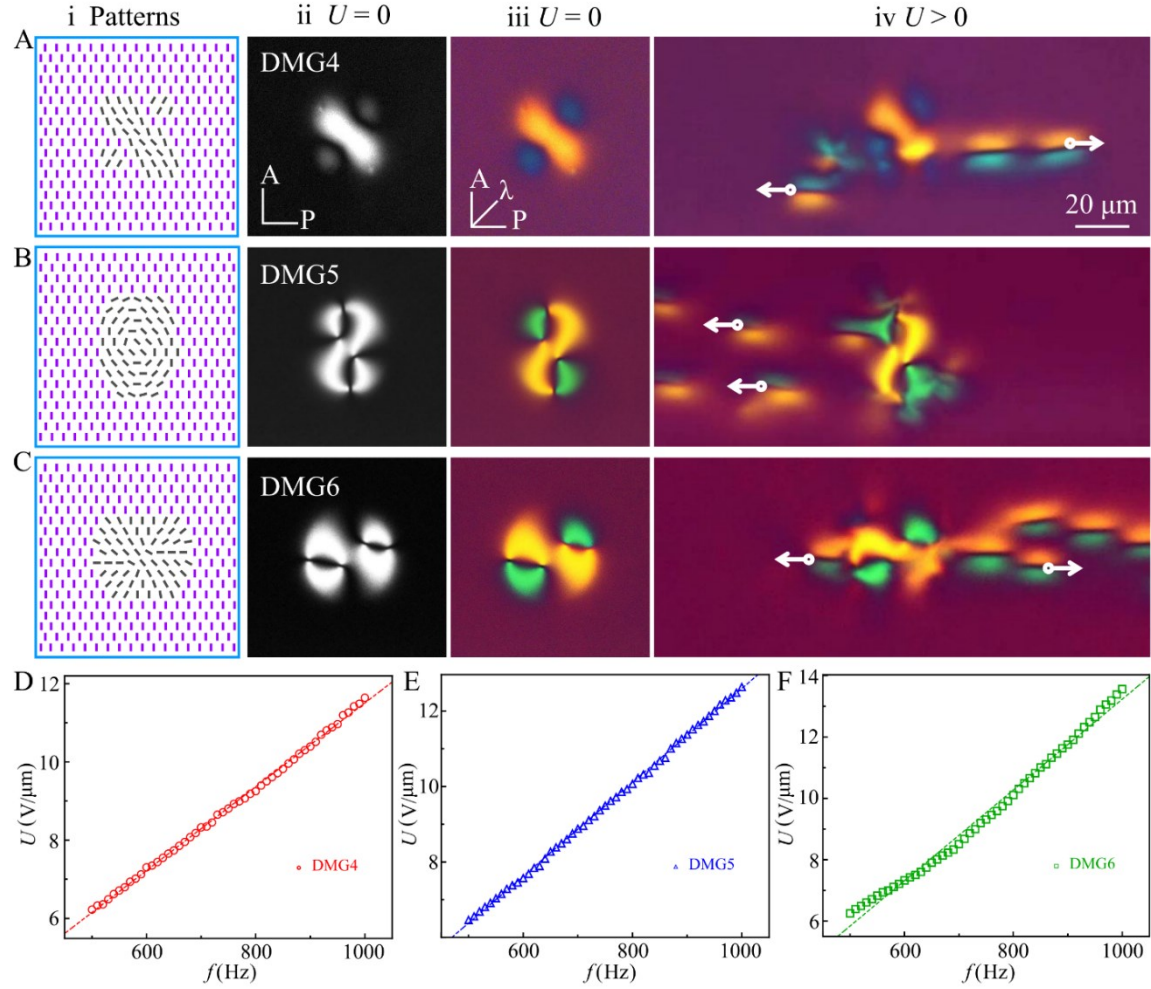


Fig. S3. Directrons machine guns with various director profiles. (A) The DMG4 (cell thickness: $d = 8.2 \mu\text{m}$, electric field: $f = 520$ Hz, $U = 52.1$ V). (B) The DMG5 ($d = 8.1 \mu\text{m}$, $f = 990$ Hz, $U = 101.1$ V). (C) The DMG6 ($d = 8.2 \mu\text{m}$, $f = 500$ Hz, $U = 51.3$ V). (i) The director distributions of three DMGs. (ii) Polarizing microscopy textures under crossed polarizers, $U = 0$. (iii) Polarizing microscopy textures under crossed polarizers and a compensator ($\lambda = 530$ nm), $U = 0$. (iv) The domination of directrons emission by sinusoidal AC electric fields, scale bar $20 \mu\text{m}$. (D to F) Frequency dependencies of threshold voltages required to generate directrons, corresponding to (A) to (C).

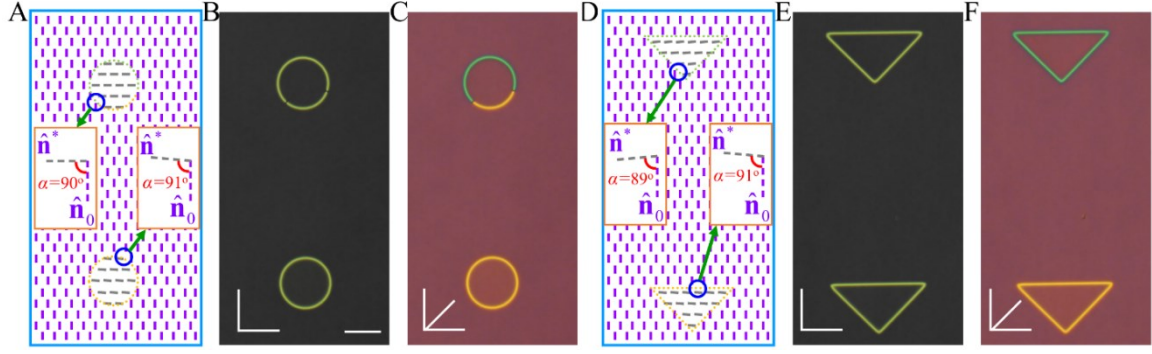


Fig. S4. Dependence of the output diagram on the angle between the directors in inner and outer pattern ($d = 8.3 \mu\text{m}$, $T = 55^\circ\text{C}$). (A) director distribution of circle domains with $\alpha = 90^\circ$ and $\alpha = 91^\circ$. α is the angle difference between inner and outer director of circular domain. (B) POM texture under crossed polarizer. (C) POM texture under crossed polarizer and a red plate compensator ($\lambda = 530 \text{ nm}$). (D) director distribution of triangle domains with $\alpha = 89^\circ$ and $\alpha = 91^\circ$. (E) POM textures under crossed polarizer. (F) POM textures under crossed polarizer and a red plate compensator ($\lambda = 530 \text{ nm}$).

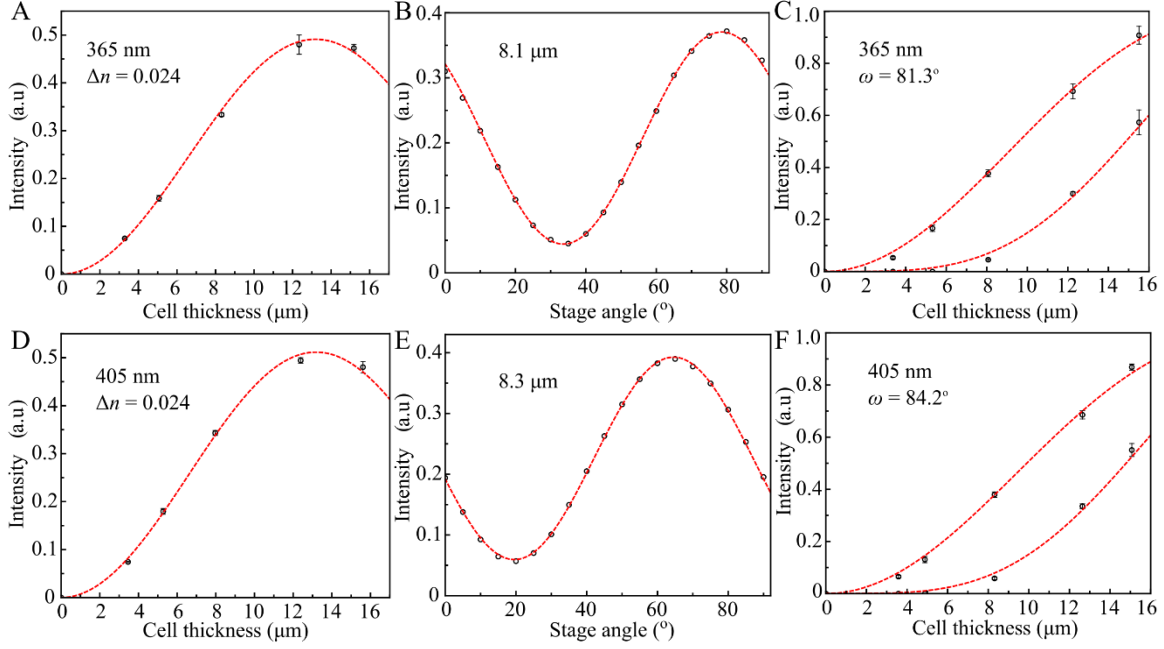


Fig. S5. Birefringence and azimuthal surface anchoring of photoaligned CCN47 in nematic phase ($T = 55^\circ\text{C}$). (A to C) data from samples exposed by light with $\lambda = 365\text{ nm}$. (A) Thickness dependences of the normalized light transmittances, the experimental data are fitted by using Equation [3] in main text with $\Delta n = 0.024$ (dashed lines). (B) Angular dependence of the normalized transmitted intensity for a cell of thickness of $8.1\text{ }\mu\text{m}$, rotated between two crossed polarizers. (C) Thickness dependences of the normalized light transmittances, the experimental data are fitted by using Equations [4] and [5] with $\Omega = 81.3^\circ$ (dashed lines). (D to F) data from samples exposed by light with $\lambda = 405\text{ nm}$. (D) Thickness dependences of the normalized light transmittances, the experimental data are fitted by using Equation [3] in main text with $\Delta n = 0.024$ (dashed lines). (E) Angular dependence of the normalized transmitted intensity for a cell of thickness $8.3\text{ }\mu\text{m}$, rotated between two crossed polarizers. (F) Thickness dependences of the normalized light transmittances, the experimental data are fitted by using Equations [4] and [5] with $\Omega = 84.2^\circ$.

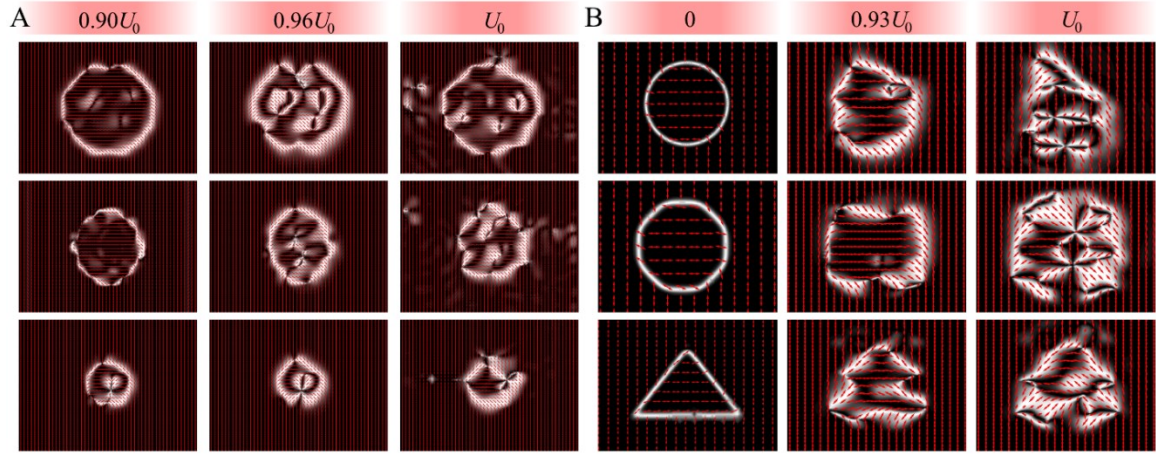


Fig. S6. Simulation results aligned with electrical controlled localization and emission of directrons. (A) directrons nucleate within the circular domains with three distinct diameters: $150\text{ }\mu\text{m}$, $75\text{ }\mu\text{m}$, and $20\text{ }\mu\text{m}$ at $0.90U_0$. More directrons appear with the elevating of voltage and then directrons escape from the confining domain and travel freely to the uniform surrounding uniform media at U_0 . (B) no directrons exist when the voltage is zero and directrons survive within the confining domains with three distinct shapes: circle, polygon, and triangle with the increase of voltage.

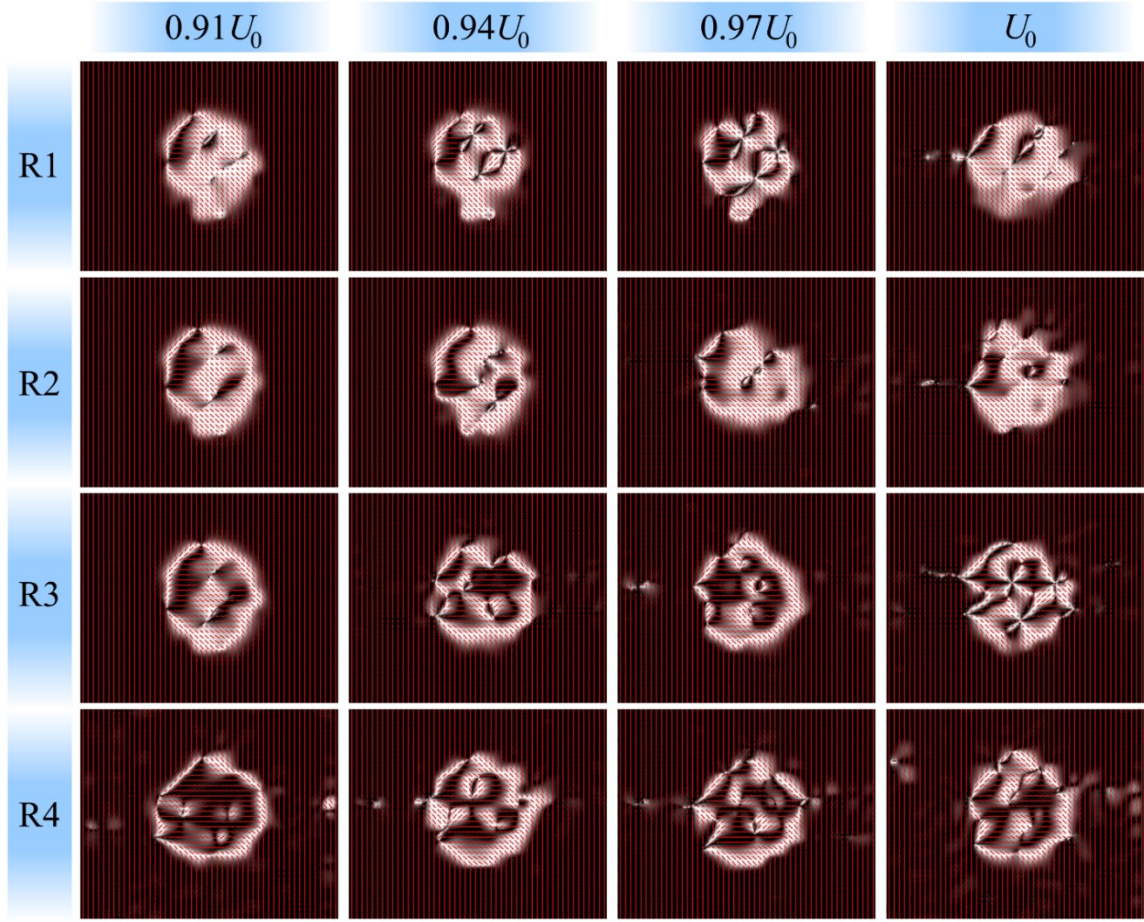


Fig. S7. Simulation outcomes corresponding to the effect of orientation variance between areas. Circular DMGs R1, R2, R3, and R4 characterized by orientation differences α_i of 45° , 60° , 75° , and 90° , respectively. The threshold voltage for directrons escaping from the DMGs R1 to R4 are $0.91U_0$, $0.94U_0$, $0.97U_0$, and U_0 , respectively.

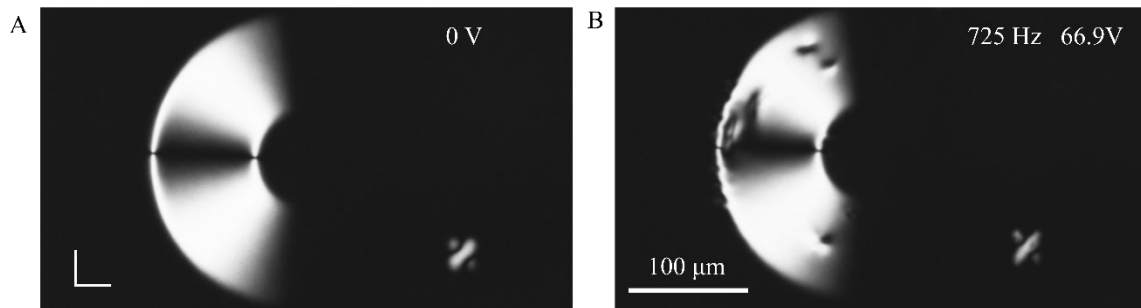


Fig. S8. Comparison of soliton generation in patterns with and without defects. (A) Patterns are observed between crossed polarizers without applied field. (B) Solitons nucleate from pattern with defect rather than pattern without defect ($f = 725$ Hz , $U = 66.9$ V , 55°C , $d = 8.1$ μm).

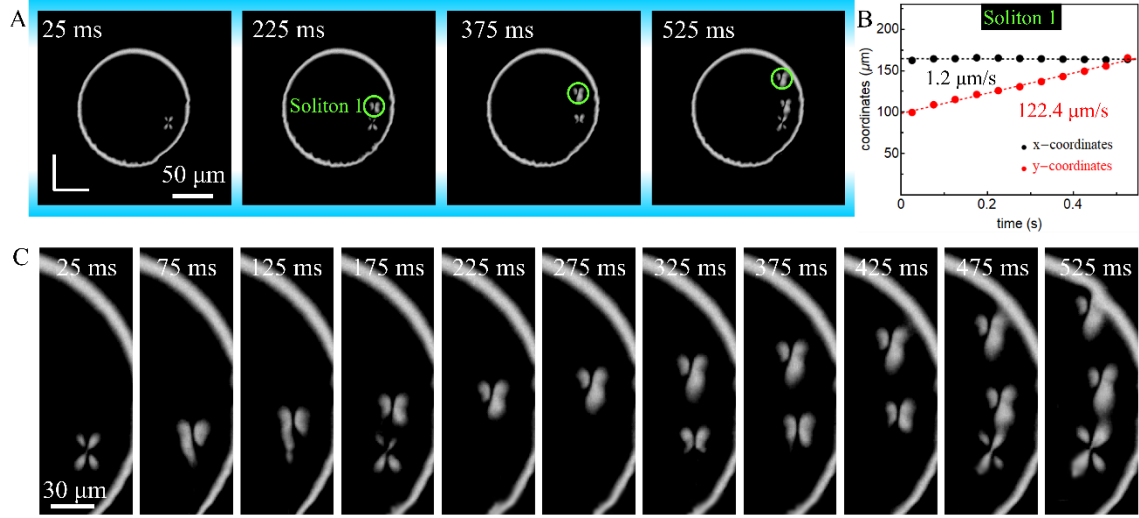


Fig. S9. Generation of directrons from bulk within the inner area. (A) Emergence and movement of directrons are observed between crossed polarizers ($f = 700 \text{ Hz}$, $U = 63.2 \text{ V}$, 55°C , $d = 7.9 \mu\text{m}$). (B) Time dependence of the x and y-coordinates of soliton 1. (C) Time evolution of directrons generation.

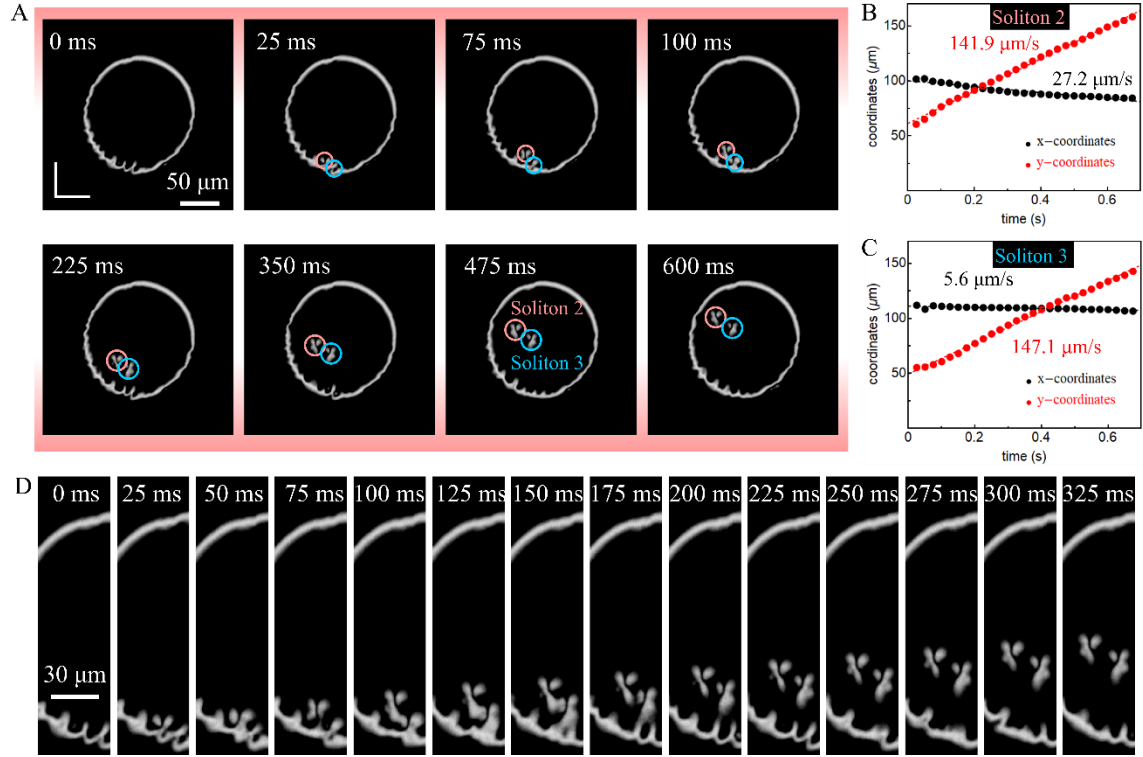


Fig. S10. Generation of directrons from the orientational boundary between two domains. (A) Emergence and movement of directrons are observed between crossed polarizers ($f = 800$ Hz, $U = 70.9$ V, 55°C , $d = 7.9$ μm). (B and C) Time dependence of the x and y-coordinates of soliton 2 and 3. (D) Time evolution of directrons generation.

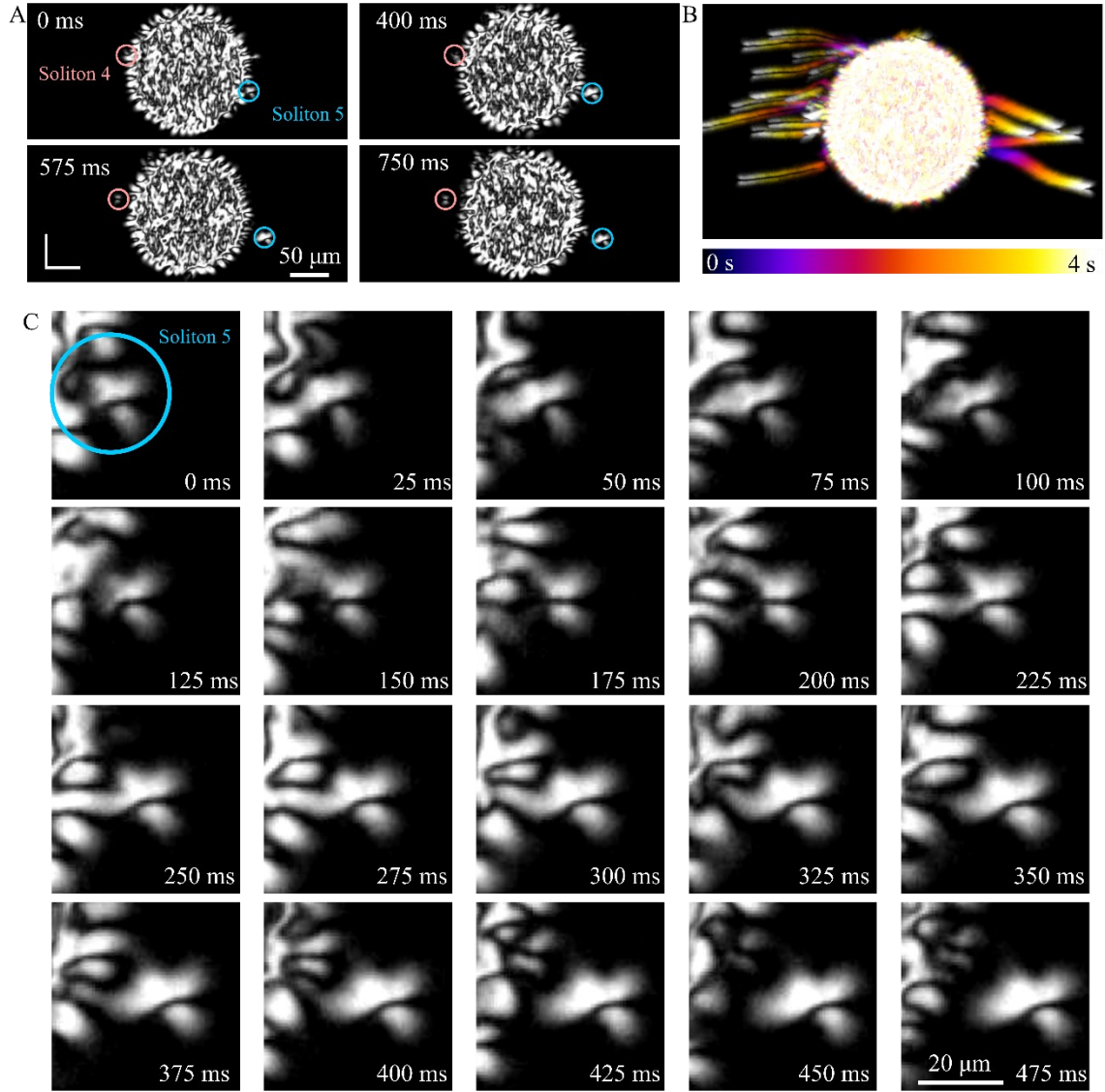


Fig. S11. Emission of directrons from the orientational boundary between two domains. (A) Emergence and movement of directrons are observed between crossed polarizers ($f = 800$ Hz , $U = 79.1$ V , 55°C , $d = 7.9$ μm). (B) Typical time-dependent trajectories of solitons. (C) Time evolution of emission of soliton 5.

Movie S1 (separate file).

Generation of directrons from the distortion with four segments

The applied electric field is $f = 550$ Hz , $U = 56.7$ V ; the cell thickness is $d = 8.1$ μm .

Real time video rate.

Movie S2 (separate file).

Generation of directrons from a pair of $+\frac{1}{2}$ and $-\frac{1}{2}$ defects within a rectangular area

The applied electric field is $f = 650$ Hz , $U = 61.4$ V ; the cell thickness is $d = 8.0$ μm .

Real time video rate.

Movie S3 (separate file).

Generation of directrons from a pair of $+\frac{1}{2}$ and $-\frac{1}{2}$ defects within a toroidal shape

Toroidal shape pattern produces directrons and guides them to propagate along the toroidal trajectory inside the pattern. The applied electric field is $f = 680$ Hz , $U = 62.9$ V ; the cell thickness is $d = 7.8$ μm . Real time video rate.

Movie S4 (separate file).

Electrical control of localization and emission of directrons in patterns with different diameters

The localization and emission of directrons in circular patterns with different diameters (150 μm , 75 μm , and 20 μm), $f = 500$ Hz , $d = 7.9$ μm . The applied voltages are $U = 46.6$ V , $U = 48.4$ V , and $U = 51.2$ V , respectively. Real time video rate.

Movie S5 (separate file).

Electrical control of localization of directrons in various patterns

The localization of directrons in the triangle, polygon, and circle patterns, $f = 500$ Hz , $d = 7.9$ μm . The applied voltages are $U = 45.0$ V , $U = 46.7$ V , and $U = 48.5$ V , respectively. Real time video rate.

Movie S6 (separate file).

Voltage dependence of directrons generation

The threshold voltage for the DMGs R1, R2, R3, and R4 to generate directrons are 52.5 V , 52.2 V , 51.9 V , and 51.6 V at $f = 500$ Hz ; the cell thickness is $d = 8.1 \mu\text{m}$. Real time video rate.

Movie S7 (separate file).

Simulation results of unidirectional generation of directrons

Movie S8 (separate file).

Saturation of directrons for the designed letters "NJU, UC, and NJUPT"

The applied electric field is $f = 500$ Hz , $U = 52.0$ V ; the cell thickness is $d = 8.0 \mu\text{m}$. Real time video rate.

Movie S9 (separate file).

Localization of directrons in Nanjing University Chinese Font (南京大学)

The applied electric field is $f = 500$ Hz , $U = 54.0$ V ; the cell thickness is $d = 7.9 \mu\text{m}$. Real time video rate.

SI References

1. A. Martinez, H. C. Mireles, I. I. Smalyukh, Large-area optoelastic manipulation of colloidal particles in liquid crystals using photoresponsive molecular surface monolayers. *Proc. Natl. Acad. Sci. U.S.A.* **108**, 20891-20896 (2011).
2. P.-G. de Gennes, J. Prost, *The physics of liquid crystals* (Oxford university press, Oxford, 1993).
3. H. Grebel, R. M. Hornreich, S. Shtrikman, Landau theory of cholesteric blue phases. *Phys. Rev. A* **28**, 1114 (1983).
4. J. V. Selinger, Interpretation of saddle-splay and the oseen-frank free energy in liquid crystals. *Liq. Cryst. Rev.* **6**, 129-142 (2018).
5. H. Mori, E. C. Gartland Jr., J. R. Kelly, P. J. Bos, Multidimensional director modeling using the q tensor representation in a liquid crystal cell and its application to the π cell with patterned electrodes. *Japanese Journal of Applied Physics* **38**, 135 (1999).
6. J. Nehring, A. Saupe, Calculation of the elastic constants of nematic liquid crystals. *Journal of Chemical Physics* **56**, 5527-5528 (1972).
7. L. D. Landau, E. M. Lifshitz, *Fluid mechanics: Landau and Lifshitz: Course of theoretical physics* (Elsevier, 2013), volume. 6.
8. T. Porenta, M. Ravnik, S. Zumer, Effect of flexoelectricity and order electricity on defect cores in nematic droplets. *Soft Matter* **7**, 132-136 (2011).
9. L. A. Parry-Jones, R. B. Meyer, S. J. Elston, Mechanisms of flexoelectric switching in a zenithally bistable nematic device. *Journal of Applied Physics* **106**, 014510 (2009).
10. S. P. Palto, N. J. Mottram, M. A. Osipov, Flexoelectric instability and a spontaneous chiral-symmetry breaking in a nematic liquid crystal cell with asymmetric boundary conditions. *Phys. Rev. E* **75**, 061707 (2007).
11. M. L. Blow, M. T. T. da Gama, Interfacial motion in flexo-and order-electric switching between nematic filled states. *Journal of Physics: Condensed Matter* **25**, 245103 (2013).
12. G. Barbero, I. Dozov, J. F. Paliarne, G. Durand, Order electricity and surface orientation in nematic liquid crystals. *Phys. Rev. Lett.* **56**, 2056 (1986).
13. A.-L. Alexe-Ionescu, Flexoelectric polarization and second order elasticity for nematic liquid crystals. *Physics Letters A* **180**, 456-460 (1993).

14. O. D. Lavrentovich, Design of nematic liquid crystals to control microscale dynamics. *Liq. Cryst. Rev.* **8**, 59-129 (2020).
15. L. D. Landau *et al.*, *Electrodynamics of continuous media* (Elsevier, 2013).
16. A. J. Davidson, C. V. Brown, N. J. Mottram, S. Ladak, C. R. Evans, Defect trajectories and domain-wall loop dynamics during two-frequency switching in a bistable azimuthal nematic device. *Phys. Rev. E* **81**, 051712 (2010).
17. C. Denniston, J. M. Yeomans, Flexoelectric surface switching of bistable nematic devices. *Phys. Rev. Lett.* **87**, 275505 (2001).
18. A. J. Davidson, N. J. Mottram, Flexoelectric switching in a bistable nematic device. *Phys. Rev. E* **65**, 051710 (2002).
19. N. Sulaiman, D. Marenduzzo, J. M. Yeomans, Lattice boltzmann algorithm to simulate isotropic-nematic emulsions. *Phys. Rev. E* **74**, 041708 (2006).
20. G. P. Alexander, J. M. Yeomans, Flexoelectric blue phases. *Phys. Rev. Lett.* **99**, 067801 (2007).
21. A. V. Ryzhkova, F. V. Podgornov, W. Haase, Nonlinear electrophoretic motion of dielectric microparticles in nematic liquid crystals. *Applied Physics Letters* **96**, 151901 (2010).
22. O. D. Lavrentovich, I. Lazo, O. P. Pishnyak, Nonlinear electrophoresis of dielectric and metal spheres in a nematic liquid crystal. *Nature* **467**, 947-950 (2010).